

A highly optimized quantum algorithm for accurate simulations of dynamical impurity models on noisy quantum hardware

Thomas Steckmann,¹ Trevor Keen,² Alexander F. Kemper,¹ Eugene F. Dumitrescu,³ and Yan Wang³

¹*Department of Physics, North Carolina State University, Raleigh, North Carolina 27695, USA*

²*Department of Physics and Astronomy, University of Tennessee, Knoxville, TN 37996*

³*Quantum Computational Science Group, Oak Ridge National Laboratory, Oak Ridge, Tennessee 37831, USA*

(Dated: November 24, 2021)

Dynamical mean-field theory (DMFT) maps the local Green's function of the Hubbard model onto that of the Anderson impurity model. Quantum algorithms have been proposed to efficiently solve impurity models by preparing and evolving the ground state under the impurity Hamiltonian, which is the most expensive part of the calculation for DMFT. We propose a highly optimized fast-forwarding quantum circuit to significantly improve quantum algorithms for the minimal DMFT problem. Our Cartan decomposition-based algorithm uses a fixed depth quantum circuit to eliminate time-discretization errors and evolve an initial state over *arbitrary* time. Exploiting the structure of the fast-forwarding circuits, we sufficiently reduce the gate cost to simulate the dynamics of, and extract frequencies from, the Anderson impurity model on noisy quantum hardware and demonstrate the Mott transition. Especially near the Mott phase transition when the quasiparticle resonance frequency approaches zero and evolving the system over long-time scales is necessary, our method maintains accuracy where Trotter error would otherwise dominate. By accurately computing the DMFT phase diagram on a digital computer we open up the way for more sophisticated techniques to solve more complex correlated electronic phenomena.

I. INTRODUCTION

Using quantum computers to accurately model the behaviour of strongly correlated quantum systems is one of the most promising near-term applications of noisy intermediate scale quantum (NISQ) computers. Shor's algorithm [1] for factoring large numbers will require thousands of near-noiseless qubits to become practically useful. On the other hand, quantum simulations of fermions only require ~ 100 qubits to potentially surpass classical simulation methods. Proposals for simulating correlated fermionic systems using quantum computers exist [2–5] but relatively few have actually implemented or tested due to the noise of current devices [6–8].

In prior work studying the dynamics of interacting electrons via dynamical mean-field theory (DMFT), it was observed that even over very small time scales Trotter approximate time evolutions lead to nonphysical results: comparing to theoretical values, simulations on the quantum computer give inaccurate frequencies of the time evolution for the two-site Anderson impurity model system, which are symptoms of decoherence or approximation errors [8]. For NISQ systems, the Trotter approximation leads to a dilemma: it becomes exact in the limit of an infinite-depth circuit, so more accurate simulations require increased gate counts, but increasing gate count reduces simulation fidelity due to accumulated noise. In Ref. 7, the authors use a variational quantum eigensolver (VQE) to implement an exact diagonalization solver for the two-site DMFT problem. This method works well for two-site DMFT after a regularization technique is used to remove the unphysical pole that arises from small errors. The hardware requirements needed to achieve reliable updates in the DMFT loop using the Trotter decomposition of the time-evolution operator has been analyzed in Ref. 9.

In this work, we approach the problem of solving the two-site DMFT problem by utilizing a Lie-algebraic method to fast-forward the the dynamics of the Anderson Impurity Model (AIM). Our method, based on a Cartan decomposition of the algebraic closure of the Hamiltonian, compiles the time evolution operator into a fixed depth circuit which introduces only arbitrarily low numerical error for any chosen simulation time. As described Ref. 10 the Cartan decomposition requires finding a particular sequence of unitary rotations which, when contracted, span and parameterize the time-evolution unitary of a target system. The Cartan decomposition generalizes the polar and singular-value decompositions at the level of groups and provides a mapping from the required dynamics onto two sets of parameterized unitaries.

We first review and motivate the quantum impurity model and provide a hybrid quantum-classical algorithm solving it. We then apply group analysis to fast-forward the dynamical simulation on a quantum computer. The structure of

This manuscript has been authored by UT-Battelle, LLC, under Contract No. DE-AC0500OR22725 with the U.S. Department of Energy. The United States Government retains and the publisher, by accepting the article for publication, acknowledges that the United States Government retains a non-exclusive, paid-up, irrevocable, world-wide license to publish or reproduce the published form of this manuscript, or allow others to do so, for the United States Government purposes. The Department of Energy will provide public access to these results of federally sponsored research in accordance with the DOE Public Access Plan.

Cartan decomposition allows for further simplifications which result in a highly optimized circuit that can be tailored to execute on specific hardware architectures. We then extract accurate ultra-low frequency signals from simulations of the two-site DMFT on NISQ systems and demonstrate the first Mott-insulating phase transition in the Hubbard model in a digital quantum simulation.

II. MODEL HAMILTONIANS

A. The Hubbard model

Although it is one of the simplest to express models that capture interactions between electrons, the Fermi-Hubbard model has no known exact solution in more than one dimension. Despite its relative simplicity, the Hubbard model accounts for many interesting phenomena in condensed matter physics, including the Mott metal-insulator transition [11–13], antiferromagnetism [14], emergent spin and stripe orders [15, 16], strange metallic behavior [17], pseudogaps [18, 19], and high-temperature superconductivity [18, 20].

The single-band Hubbard model Hamiltonian in one dimension is given by

$$\hat{H}_{\text{Hubbard}} = -\tilde{t} \sum_{\langle i,j \rangle, \sigma} (\hat{c}_{i\sigma}^\dagger \hat{c}_{j\sigma} + \hat{c}_{j\sigma}^\dagger \hat{c}_{i\sigma}) + U \sum_i \hat{n}_{i\uparrow} \hat{n}_{i\downarrow} - \mu \sum_{i,\sigma} \hat{n}_{i,\sigma}, \quad (1)$$

where $\hat{c}_{i\sigma}^\dagger$ ($\hat{c}_{i\sigma}$) is the electron creation (annihilation) operator for electron with spin $\sigma \in \{\uparrow, \downarrow\}$ at lattice site i ; $\hat{n}_{i\sigma} = \hat{c}_{i\sigma}^\dagger \hat{c}_{i\sigma}$ is the electron density operator; \tilde{t} is the hopping integral (“tunneling”) which we typically choose as units of energy by setting $\tilde{t} = 1$; U models the Coulomb interaction with a double occupancy delta function interaction; and μ is the chemical potential. Here, $\langle i, j \rangle$ refers to indices of nearest-neighbor sites on the lattice [21]. The Hubbard model has been recently investigated in the context of quantum computing with applications to VQE algorithms [22, 23] and as a benchmarking quantum simulations [4, 24, 25].

B. Anderson impurity model and dynamical mean-field theory

Exact simulations of the Hubbard model in the general case are limited to dozens or hundreds of particles [26, [\[YW: or any other state-of-the-art work to be cited here?\]](#)], far from the large number of particles which would be considered in the macroscopic (thermodynamic) limit. Dynamical mean-field theory is a significant development in studying the Hubbard model for such large systems. [27] In the limit of a lattice with infinite dimensions (∞ - d), such as ∞ - d hypercubic Bethe lattice with infinite coordination number, DMFT exactly maps the solution of the Hubbard model to that of the Anderson impurity model, where the temporal correlations are accurately captured. The interacting electrons in the Hubbard model in the thermodynamic limit (i.e., *infinite* lattice sites) is reduced to electrons interacting on a single quantum impurity site coupled to an electronic bath of *continuous* levels that tunnel into the impurity site. In numerical simulations, we describe the energy levels as discrete bath lattice sites with on-site energy ϵ_i and index $i \in \{1, \dots, N_b\}$. For the nonmagnetic states we consider, these parameters do not depend on the electron spin quantum number. The Anderson impurity model Hamiltonian is given by

$$\hat{H}_{\text{AIM}} = \sum_{i=1, \sigma}^{N_b} V_i (\hat{c}_{0,\sigma}^\dagger \hat{c}_{i,\sigma} + \hat{c}_{i,\sigma}^\dagger \hat{c}_{0,\sigma}) + U \hat{n}_{0,\uparrow} \hat{n}_{0,\downarrow} + \sum_{i=0, \sigma}^{N_b} (\epsilon_i - \mu) \hat{n}_{i,\sigma}, \quad (2)$$

where V_i is the coupling (tunneling) between the impurity site (site index 0) and bath sites. The Coulomb interaction (U) term only involves the impurity site. In numerical simulation, the bath continuum is approximated by a discrete collection of bath sites. The minimal approximation is a two-site DMFT, which includes a single bath site ($N_b = 1$) and a single impurity site.

Using X_i, Y_i, Z_i to denote the Pauli operator acting on site i . A Jordan-Wigner spin-fermion transformation (Appendix A) maps the AIM Hamiltonian to the Pauli-Hamiltonian

$$\hat{H}_{\text{AIM}} = \frac{V}{2} (X_0 X_1 + Y_0 Y_1 + X_2 X_3 + Y_2 Y_3) + \frac{U}{4} Z_0 Z_2. \quad (3)$$

In classical computation, even though the DMFT impurity mapping simplifies the problem, simulations based on exact diagonalization are still limited to ~ 20 sites [28] due to the exponential growth of the Hilbert space, and thus

the exponential amount of memory required to store the quantum many-body state. Other methods, such as quantum Monte Carlo (QMC) [29] and matrix product state (MPS) [30] methods, also suffer from some sort of exponential complexity scaling making them intractable. In the case of QMC, the fermion sign problem [31] has been shown to be NP-hard in general and limits simulations to high temperatures. Matrix product state methods, on the other hand, suffer from entanglement issues for certain geometries [30]. Quantum computers alleviate this exponential scaling by instead storing many-body quantum states with memory resources scaling polynomially with the system size.

III. ALGORITHM AND METHODS

A. Algorithm for computing Green's function

In DMFT, the dynamics and response of the interacting electron system is described by the *retarded impurity Green's function* which is denoted as $G_{\text{imp}}^R(t)$ in the time domain. This Green's function describes the propagation of a perturbation of the system as the system evolves. In our case, which is Green's function at zero temperature, we consider injecting (removing) a particle from the ground state of the system and, after the perturbation is removed by removing (injecting) a particle, measuring the overlap of the ground state and the final state over time. The impurity Green's function refers to injecting or removing the particles at the impurity site. In this case, there are two possibilities, injecting or removing a spin- \uparrow particle or a spin- \downarrow particle, corresponding to the spin- \uparrow and spin- \downarrow impurity Green's functions, respectively. The half-filled ground state has zero total spin and is spin-rotationally invariant, so spin- \uparrow and spin- \downarrow perturbations behave identically. This is known as spin-rotational symmetry. Therefore, we give the impurity Green's function without spin label in terms of fermion operators that has an unspecified spin index σ as follows.

$$G_{\text{imp}}^R(t, t') = -i\theta(t - t') \langle \psi_0 | \{ \hat{c}_{0,\sigma}(t), \hat{c}_{0,\sigma}^\dagger(t') \} | \psi_0 \rangle \quad (4)$$

In the Heisenberg picture, operators $\hat{c}(t)$ are time evolved as $\hat{c}(t) = U^\dagger(t) \hat{c} U(t) = e^{it\hat{H}} \hat{c} e^{-it\hat{H}}$. To simplify the computation, we set $t' = 0$. In Appendix A we elaborate on the full expansion and subsequent simplification of Green's function after the Jordan-Wigner transform is applied, which results in the relatively inexpensive summation over only the real component

$$iG_{\text{imp}}^R(t > 0) = \text{Re}[\langle \psi_0 | U^\dagger(t) X_0 U(t) X_0 | \psi_0 \rangle] \quad (5)$$

This term can be evaluated as the expectation of a single Hadamard-test type quantum circuit using only one time evolution operator in the circuit.

1. Iteration loop for DMFT

The DMFT mapping is a self-consistent mapping, and thus requires multiple iterations where the DMFT parameters V_i and ϵ_i are updated from initial guesses in the Anderson impurity model depending on the parameters of the original lattice model until the system reaches self-consistency. For each iteration, the V_i and ϵ_i computed at end of the previous iteration are put into the impurity model, which is then solved, and the solution is used to recompute the DMFT parameters. The iteration loop continues until the recomputed values are sufficiently close to the previous values of V_i and ϵ_i . For the two-site model, particle-hole symmetry and knowledge of the general form for the solution provide a mechanism for reducing the cost of the computation and the accuracy of convergence. The form of the DMFT loop used for our calculations can be summarized as follows and is represented in Fig. 1:

1. Choose initial values for parameters V_i and ϵ_i . Due to half-filling of the two-site model, the values for ϵ_0 and ϵ_1 can be fixed such that they simplify the form of the Hamiltonian, i.e. we can let $\epsilon_0 = 0$ and $\epsilon_1 = \frac{U}{2}$.
2. Evaluate the retarded impurity Green's function $G_{\text{imp}}^R(t)$ over a selection of time t values. In the two-site model, the evaluated function will have the form

$$-iG_{\text{imp}}^R(t > 0) = 2[\alpha_1 \cos(\omega_1 t) + \alpha_2 \cos(\omega_2 t)] \quad (6)$$

where ω_1 is the quasi-particle resonance frequency [32].

3. Compute the discrete Fourier transform (DFT) of Green's function: $G_{\text{imp}}^R(\omega)$.

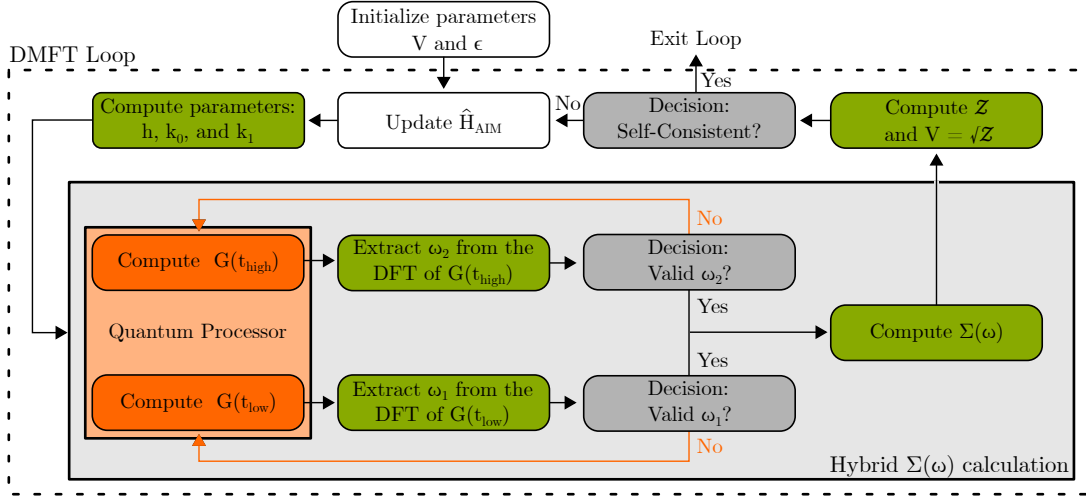


FIG. 1: Diagram of the DMFT loop, as implemented in the two-site calculation. Our procedure initialized $V = 0.5$, and for each DMFT loop iteration recomputes the parameters for the Cartan decomposition for the new value of V . The hybrid computation of $\Sigma(\omega)$ evaluates the two frequencies ω_1 and ω_2 separately, in a procedure that is elaborated on in section IV(C).

4. Compute the self-energy $\Sigma_{\text{imp}}(\omega)$ using $G_{\text{imp}}^R(\omega)$. We have the general result [33]

$$G_{\text{imp}}^R(\omega) = \frac{1}{\omega + i\delta - (\epsilon_0 - \mu) - \Delta(\omega) - \Sigma_{\text{imp}}(\omega)}. \quad (7)$$

which introduces an artificial broadening term $i\delta$. $\Delta(\omega)$ is the mean-field-like hybridization function

$$\Delta(\omega) = \frac{V^2}{\omega - (\epsilon_1 - \mu)}. \quad (8)$$

Dyson's equation $G_{\text{imp}}^R(\omega) = G_{\text{imp}}^{R(0)}(\omega) + G_{\text{imp}}^{R(0)}(\omega)\Sigma_{\text{imp}}(\omega)G_{\text{imp}}^R(\omega)$, along with the result in Eq. (7) provides an analytic solution

$$\Sigma_{\text{imp}}(\omega) = \frac{1}{G_{\text{imp}}^{R(0)}(\omega)} - \frac{1}{G_{\text{imp}}^R(\omega)}, \quad (9)$$

Here, $G_{\text{imp}}^{(0)}(\omega)$ is the non-interacting Green's function with $U = 0$. In the frequency domain, this is exactly

$$G_{\text{imp}}^{R(0)}(\omega) = \frac{1}{\omega - (\epsilon_0^{(0)} - \mu^{(0)}) - \Delta(\omega)} = \frac{1}{\omega - \Delta(\omega)}. \quad (10)$$

5. From the self-energy, compute the quasi-particle weight \mathcal{Z} and update $V_{\text{new}} = \sqrt{\mathcal{Z}}$. In this work, we use the value of the quasi-particle weight computed using the derivative of the self-energy at zero frequency:

$$\mathcal{Z}^{-1} = 1 - \left. \frac{d\text{Re}[\Sigma_{\text{imp}}(\omega)]}{d\omega} \right|_{\omega=0} \quad (11)$$

Prior work on this topic by Keen *et al.* [8] instead computed the quasi-particle weight as the integral of the spectral function $A(\omega) = -\frac{1}{\pi}\text{Im}[G_{\text{imp}}^R(\omega)]$ over the low frequency peaks

$$\mathcal{Z} = \int_{|\omega \pm \omega_1| < 4\delta} A(\omega) d\omega, \quad (12)$$

which they claimed is a better approach due to noisy results, but we determined that the difficulty in computing

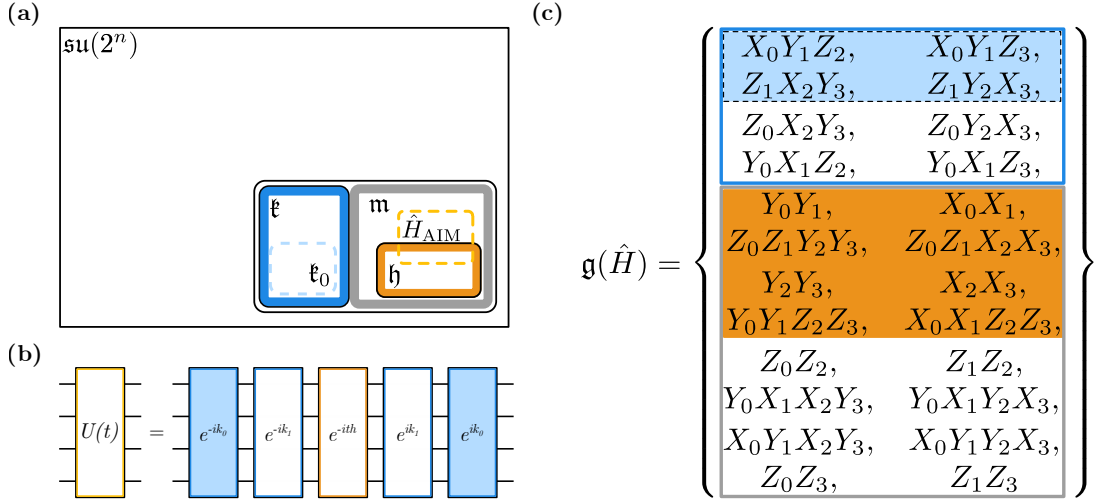


FIG. 2: (a) A generalized diagram of the Cartan decomposition of the Hamiltonian algebra with dimension = 24 within the special unitary algebra with dimension = 255. Here, \mathfrak{k}_0 is the set of basis elements which commute with X_0 , which is not a typical requirement of Cartan decomposition but results in a significant gate cost reduction in our application. (b) A block circuit diagram of the decomposed time evolution operator. (c) Cartan decomposition applied to the AIM Hamiltonian Eq. (2), where the blue, shaded light blue, gray, and shaded orange color regions correspond to the sets \mathfrak{k} , \mathfrak{k}_0 , \mathfrak{m} , and \mathfrak{h} .

\mathcal{Z} using Eq. (11) instead arises from the numerical instability of taking the derivative of the self-energy computed using $G_{\text{imp}}^R(\omega)$ fitted to Eq. (6) without analytically exact solutions for the parameters. Instead of computing the derivative in Eq. (11) numerically, we solve the derivative analytically by using the exact Fourier integral transform of Eq. (6), remove the unphysical simple pole of self-energy by assuming a condition obeyed by the exact solution $\frac{2\alpha_1}{\omega_1^2} + \frac{2\alpha_2}{\omega_2^2} = \frac{1}{V^2}$, and finally find Eq. (13), which is equivalent to Eq. (14) that depends only on the parameters ω_1 and ω_2 . In converting Eq. (13) to Eq. (14), we use the spectral function sum rule $2\alpha_1 + 2\alpha_2 = 1$.

$$\mathcal{Z} = \frac{2(\alpha_1 \omega_2^2 + \alpha_2 \omega_1^2)^2}{\alpha_1 \omega_2^4 + \alpha_2 \omega_1^4} \quad (13)$$

$$= \frac{\omega_1^2 \omega_2^2}{V^2(\omega_1^2 + \omega_2^2 - V^2)}. \quad (14)$$

2. Cartan decomposition

Our primary contribution is simplifying the time evolution unitary operation $\exp(-it\hat{H}_{\text{AIM}})$ in Green's function measurement circuit by applying Cartan decomposition. The standard method based on Trotterization is an approximation of the time evolution circuit which converges in the limit of an infinite depth circuit. Though there are different methods of approaching a Trotter time evolution, the first order approximation is typically applied [8, 9, 33]:

$$e^{-it\hat{H}} = \left(e^{-i\frac{t}{N}\hat{H}} \right)^N \approx \left(\prod_{l=1}^M e^{-i\frac{t}{N}\hat{H}_l} \right)^N \quad (15)$$

where $\hat{H} = \sum_{l=1}^M \hat{H}_l$.

For Cartan decomposition, we apply the algorithm described by Kökcü *et al.* [10] and Sá Earp and Pachos [34] to exactly fast-forward the computation of Green's function using a fixed depth quantum circuit. Here, we briefly summarize the algorithm applied to \hat{H}_{AIM} given in Eq. (3) and also illustrate the steps in Fig. 2. The algorithm is implemented in our Cartan Quantum Synthesizer Python package [35]. The general outline of the Cartan form of the time-evolution operator is enumerated here:

1. Generate the *Hamiltonian algebra* $\mathfrak{g}(\hat{H})$, which is a Lie algebra over the field \mathbb{R} and is the closure under

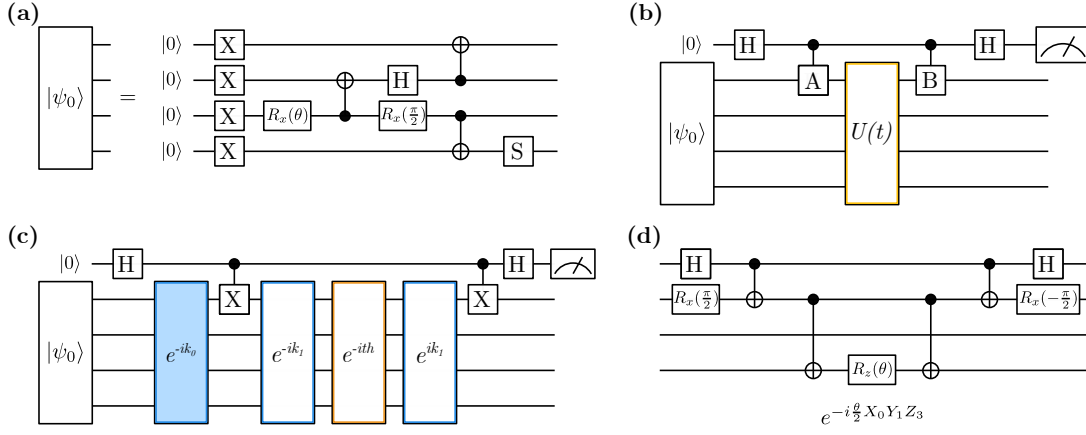


FIG. 3: (a) Ansatz circuit used to prepare the ground state. (b) General Hadamard interference type circuit used to compute $\text{Re}[\langle B(t)A \rangle]$. (c) Block decomposed Green's function circuit used in the final computation, except for the ordering and coefficients of the \mathfrak{k} and \mathfrak{h} exponentials. The property of k_0 allows for commuting through the CNOT gate so it need only be implemented once. (d) A general circuit showing the implementation of a Pauli gate exponential.

commutation of the n -qubit Pauli string basis elements of the Hamiltonian. This forms a subalgebra of $\mathfrak{su}(2^n)$.

2. Apply a Cartan involution for $g \in \mathfrak{g}(\hat{H})$, $\theta(g) = -g^T$, which partitions the Hamiltonian algebra into the subsets of symmetric operators $\mathfrak{m} : \{m \in \mathfrak{m} \mid \theta(m) = -m\}$ and skew-symmetric operators $\mathfrak{k} : \{k \in \mathfrak{k} \mid \theta(k) = -k\}$. Any other Cartan involution in which $\theta(i\hat{H}) = -i\hat{H}$ is suitable. This results in a Cartan decomposition, which obeys

$$[\mathfrak{m}, \mathfrak{m}] \subseteq \mathfrak{k}, \quad [\mathfrak{k}, \mathfrak{k}] \subseteq \mathfrak{k}, \quad [\mathfrak{m}, \mathfrak{k}] \subseteq \mathfrak{m}. \quad (16)$$

3. From \mathfrak{m} find a maximal commuting subalgebra \mathfrak{h} , which is called a *Cartan subalgebra*.
4. Find a local extremum over the algebra \mathfrak{k} of $f(K) = \langle e^{ik}(v)e^{-ik}, \hat{H} \rangle$. Here, $\langle a, b \rangle$ is the Killing form equal to $2 \times 2^n \text{Tr}(ab)$ on n qubits, and v is defined in this work as $v = \sum_i \gamma^i h_i$ where h_i are the Pauli strings which form a basis for \mathfrak{h} and γ is a transcendental number such as π .
5. Compute the vector $h = e^{-ik}(\hat{H})e^{ik}$

The results of the algorithm are the vectors $h \in \mathfrak{h}$ and $k \in \mathfrak{k}$ which satisfy $e^{-it\hat{H}} = e^{ik}e^{-ith}e^{-ik}$. Often, additional decomposition is required for e^{ik} , but in the case of two-site DMFT the elements of k commute. Because h is also composed of commuting elements, the full exponential is relatively simple to implement exactly on a quantum computer.

We note that the dimensionality of the Hamiltonian algebra generated by the \hat{H}_{AIM} scales exponentially with the number of bath sites. However, for the two-site model, the size of the algebra remains manageable. It is of continuing interest to determine if the dimensionality of the Hamiltonian algebra can be constrained to polynomial in the number of bath sites by adopting some effective approximate algorithm.

IV. HARDWARE IMPLEMENTATION

A. Circuit Components

The **ground state** was initialized using the ansatz circuit in figure 3(a) requires only a single variational parameter and 3 nearest neighbor CNOTs to prepare the ground state for any value of V or U and is the simplest known circuit to prepare the required states. The value θ is determined by minimizing the energy through a simulated Variational Quantum Eigensolver. To compute the expectation of **Green's function** $\text{Re}[\langle X(t)X \rangle]$, Eq. (5), we use the circuit in figure 3(b) [8, 33]. The circuit introduces an ancilla and adds only 2 CNOT gates to the simulation. The expectation $\text{Re}[\langle \hat{B}(t)\hat{A} \rangle]$ is computed as the expectation of the measurement on the ancilla $\langle Z_a \rangle = \text{Pr}(0_a) - \text{Pr}(1_a)$. Measuring the imaginary component, which is unnecessary in our particular application, can be accomplished by

measuring $\langle Y_a \rangle$, requiring only an $R_x(\pi/2)$ gate after the final Hadamard gate. Implementing the **time evolution** component of figure 3(b) requires first generating the coefficients for k_0 , k_1 , and h for a given U and V using the optimizer implemented in the Cartan Quantum Synthesizer [35]. Green's function can be computed at any time with independent, arbitrarily low numerical error.

The full circuit, shown in figure 3(c), follows from the fact that the elements of k_0 commute with X_0 and thus the X_0 in Green's function.

$$\begin{aligned} \langle U(-t)X_0U(t)X_0 \rangle &= \langle e^{ik_0}e^{ik_1}e^{ith}e^{-ik_1}e^{-ik_0}X_0e^{ik_0}e^{ik_1}e^{-ith}e^{-ik_1}e^{-ik_0}X_0 \rangle \\ &= \langle e^{ik_0}|e^{ik_1}e^{-ith}e^{-ik_1}X_0(e^{-ik_0}e^{ik_0})e^{ik_1}e^{-ith}e^{-ik_1}X_0|e^{-ik_0} \rangle \end{aligned} \quad (17)$$

So instead of preparing as the initial state $|\psi_0\rangle$, we prepare $e^{-ik_0}|\psi_0\rangle$ and time evolve using $e^{ik_1}e^{-ith}e^{-ik_1}$. A combination of manual and algorithmic transpiling through Qiskit reduces the full cost of the final circuit to a count of 77 nearest neighbor CNOTs [36].

B. Error Mitigation

In this work we employ three methods of error mitigation beyond the work done to reduce the circuit depth. **Randomized Cartan parameters** are employed in an effort to mitigate coherent noise, especially over rotation of the entangling gates [37]. The minimization of $f(K)$ over different initial conditions permits distinct sets of parameters k_0 and k_1 at the minimum. Thus, quantitatively, we observe that averaging the results from two or more sets of Cartan parameters at each time serves to reduce the error in the evaluation. In this work, we use two different solutions to the Cartan Decomposition. The second method to reduce error, **measurement error mitigation**, serves as an initial step in correcting noise in the experiment results, and we process the quantum measurements through the native procedure in Qiskit [36, 38].

The final, and most significant error mitigation technique, follows from measurements on the primary, or wavefunction, qubits. The Hadamard test does not use or require a measurement of these qubits, instead assuming that the wavefunction qubits are traced out of the final circuit before measuring $\langle Z_a \rangle$. The partial trace operation is equivalent to simply measuring the resulting wavefunction state in the Z basis. Indeed, the final state of the wavefunction qubits is a superposition of $|\psi_0\rangle$ and $X_0(t)X_0|\psi_0\rangle$, both of which we expect to have the same particle number and total spin as the original state $|\psi_0\rangle$. The initial state is known to have two fermions with a total spin zero, so for each shot in the evaluation of Green's function, we evaluate if the final measurement of the wavefunction state maintains both parameters: discarding the shot if either condition is violated. This corresponds to checking for some odd bit-flip error in the wavefunction qubits which we expect to affect the final ancilla measurement. On `imbq_manila`, approximately 65% of the circuit evaluations are discarded due to this correction, which is applied after all other error mitigation techniques.

C. DMFT Loop

Evaluation of Green's function and the convergence of the DMFT loop requires minimizing errors and evaluating a series of discrete time points sufficient to determine both ω_1 and ω_2 . Generally, these two criteria are contradictory to a third consideration of the run-time for the evaluation. That is, increasing the number of shots, the number of randomized Cartan parameters, and the discrete time points evaluated corresponds to increasing accuracy in convergence but significantly increased run-time. We determine that 16,000 shots split between two sets of Cartan parameters to have sufficiently low errors after mitigation efforts. Above the critical $U_c = 6$, the frequency ω_1 at self-consistency converges to 0. For any set of time steps t_H with a nyquist frequency above the high frequency $\omega_2 = \frac{U}{2}$ at self-consistency, sampling at a long enough time to determine, for example, $\omega_1 = .01 \pm 0.005$ for $U = 8$ requires 1600 evaluations at different times. Instead, we sample Green's function two different frequencies to evaluate ω_2 and then ω_1 separately. Due to frequency aliasing, the order of the sampling is important. Evaluating ω_2 first for permits the sampling frequency for ω_1 such that the aliased signal [39]

$$f_{\text{perceived}} = \left| f_{\text{signal}} - f_{\text{sampling}} \times \text{Nearest Integer} \left(\frac{f_{\text{signal}}}{f_{\text{sampling}}} \right) \right|, \quad (18)$$

which appears from under-sampling ω_2 , is outside the region where the frequency ω_1 is expected. Figure 4 shows the evaluation of $-\text{Im}[G^R(t)]$ in the ideal case in orange (i/ii upper) and the results from high frequency sampling for ω_2 in purple (i, lower) and ω_1 in blue (ii, lower). In each case, the t_H and t_L are evaluated at 150 values and are chosen

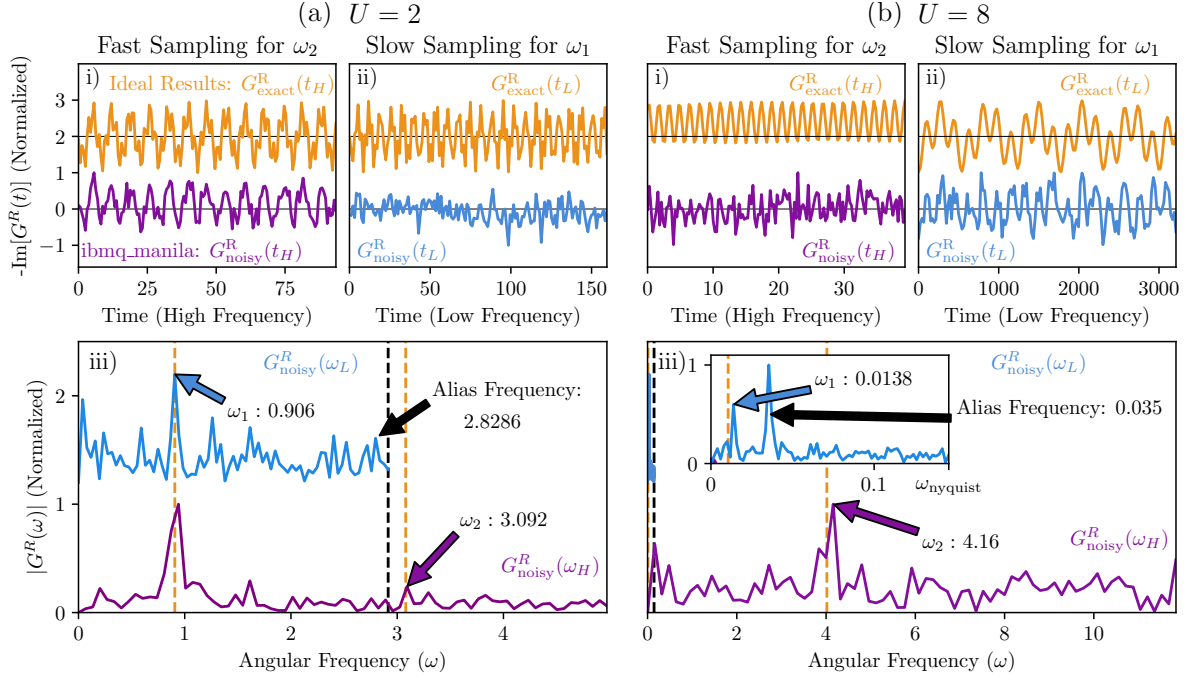


FIG. 4: Green's function sampled on the quantum computer `ibmq_manila` at self-consistency. Initial Conditions: (a) $U = 2$ and $V_{\text{initial}} = 0.964$ and (b) $U = 8$ and $V_{\text{initial}} = 0.119$. (i/ii) Normalized Green's function with a phase correction (top) and the actual, noisy results (bottom) sampled with high (t_H) and low (t_L) frequencies to evaluate ω_2 and ω_1 , respectively. (iii) The discrete Fourier transform showing the ideal frequencies (dashed, orange) and the evaluated peaks for both frequencies. Spurious peaks at $\omega = 0$ have been removed. (a) Returns a value of $V_{\text{new}} = 0.944$ and (b) returns a value of $V_{\text{new}} = 0.116$, both within the tolerance of 0.02.

with sampling frequencies between three and ten times greater (1.5 to $5 \times \omega_{\text{nyquist}}$) than the frequency of ω_2 and ω_1 determined in the previous iteration of the DMFT loop.

To prevent poor updates of the loop when an incorrect peak is found due to noise, only the frequency region around an expected peak, as determined by the previous ω_1 and ω_2 calculation, is searched for peaks. Additionally, each evaluation $-\text{Im}[G^R(t_L)]$ and $-\text{Im}[G^R(t_H)]$ has a condition to fail for not enough (0) or too many (>4) prominent frequency peaks present in the DFT, as determined by an adaptive height criteria based on the average and standard deviation of the absolute value of the DFT amplitudes. In the case a condition fails, the particular high frequency or low frequency calculation is rerun until the condition passes and \mathcal{Z} is computed. The loop is iterated until two sequential results of V are within a tolerance, in our case chosen to be 0.02. The exception is the convergence for $U = 6.5$, in which a prominent peak for ω_1 was not found after 3 attempts and the loop was terminated. This corresponds to failing to find a frequency with amplitude 10^{-4} within the signal-to-noise ratio of the quantum computer.

V. RESULTS

Figure 5 shows the phase diagram of the quasi-particle weight $\mathcal{Z}_{\text{noisy}}$ produced on quantum hardware, plotted against the exact self-consistent solutions for $\mathcal{Z}_{\text{exact}}$ [32]

$$\mathcal{Z}_{\text{exact}} = \begin{cases} \frac{36 - U^2}{36}, & U < U_c = 6 \\ 0, & U \geq 6 \end{cases} \quad (19)$$

For all values of U , the initial value of $V = 0.5$ is used and the color gradient shows the convergence toward the final value V_{noisy} , which is taken to be the average of the final two steps in the loop. For $U < U_c$, the convergence is within the tolerance $|V_{\text{noisy}} - V_{\text{ideal}}| < 0.02$ at self-consistency for V . For $U > U_c$, α_1 and ω_1 both vanish to zero, requiring both very long time simulation and a very good signal-to-noise ratio in the results to determine convergence. With

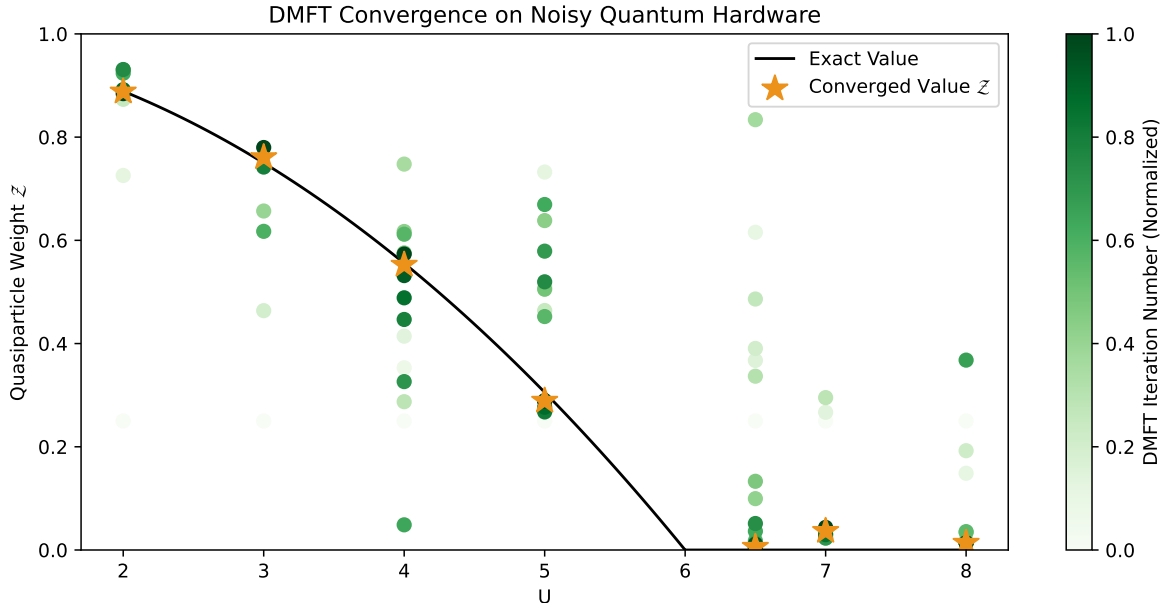


FIG. 5: DMFT phase diagram computed on a quantum computer. The solid black line corresponds to the exact value of self-consistency Eq 19, and increasing values of the iteration correspond to steps later in the DMFT loop. We have omitted from the plot values of Z which are above 1. The gap in convergence around $U_c = 6$ corresponds to the region where the critical slowing means computing the DMFT loop is cost-prohibitive.

the exception of $U = 6.5$, Z instead converges to near zero but still clearly shows the phase transition. In this regime, the fast-forwarding allowed by Cartan decomposition is essential to appropriately study the dynamics over very long times. Results for U near U_c are omitted, as critical slowing prevents convergence within a reasonable number of iteration steps. The CNOT error and coherence time values for `ibmq_manila` can be found in appendix C.

The removal of the dependence on amplitude in computing of Z is essential to the success of the DMFT calculation. The final results of the Green's function evaluation, before normalization, leads to amplitudes between 5 and 15 times lower than in the ideal case, and in general signal amplitude is not reliably preserved in the final computation. Despite this, frequency is preserved in the final signal, and thus allows for reliable updates to the DMFT loop, as shown in Figure 6. The ideal convergence [40], which is interpolated to serve as a guideline, is compared to the behavior of the convergence of the identical algorithm on a noiseless simulator and the results on quantum hardware. In the insulating phase, even on the noiseless simulator, our algorithm fails to converge exact to zero for ω_1 , again due to the vanishing amplitude of α_1 . Despite significant deviations from the ideal convergence behavior and sequential updates, the convergence on the quantum hardware trends toward self-consistency. In the case of $U = 6.5$, these deviations serve to increase the rate of convergence, but generally the deviations prevent ideal, sequential convergence in spite of the significant filtering and error mitigation.

VI. CONCLUSION

Here, we have implemented a two-site DMFT calculation on current generation superconducting quantum hardware with linear CNOT connectivity. Compared to previous methods using Trotter simulation to converge in the insulating phase and variational methods to converge in the conducting phase, our work is the first general implementation to compute the entire DMFT phase diagram [7, 8]. We found that the bottlenecks in the calculation are the noise in the quantum computer and slow convergence near the transition point. To circumvent these issues we introduced a variety of optimization and error mitigation methods including randomized Cartan parameters in the time evolution, measurement error mitigation, analysis of alias signals in the FFT, and post selection of data. The post selection of data includes enforcement of particle number and total spin conservation since the Hamiltonian under consideration cannot create/destroy particles or flip the spin of particles.

Cartan decomposition as a means of fast-forwarding time evolution serves to preserve frequency information despite

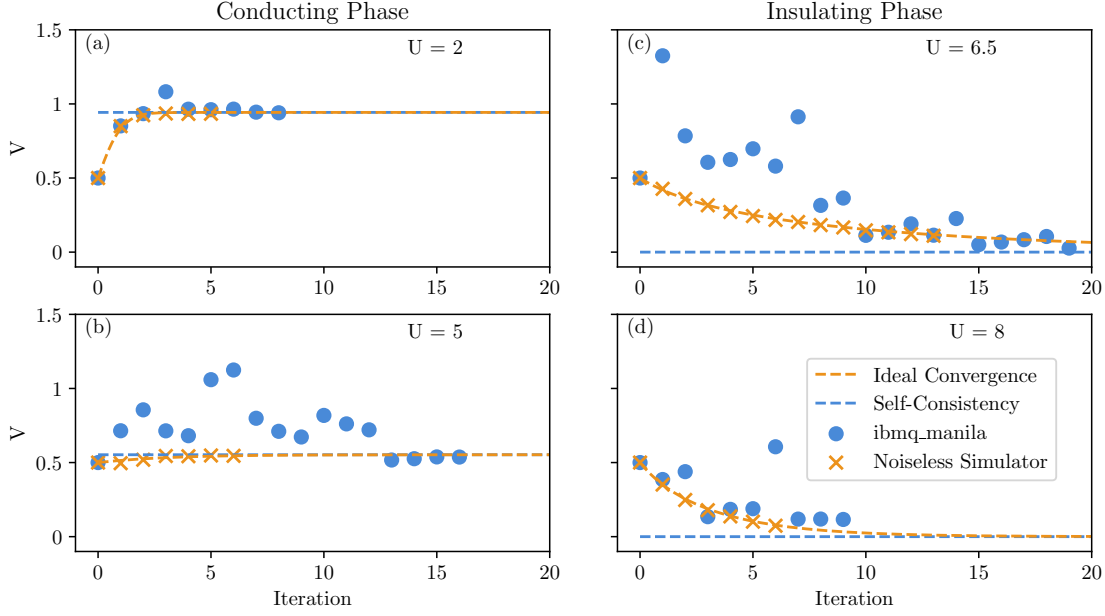


FIG. 6: DMFT step convergence behavior above (a/b) and below (c/d) critical $U_c = 6$. Despite error in the updated V , all values of converge to within the tolerance, with the except of $U = 6.5$ which terminates after no peaks near $\omega = 0$ were located.

significant noisy operation in the quantum computer, as demonstrated in this work. Although the algorithm used scales poorly with the number of lattice sites in models of interacting fermions, in such a four-qubit simulation the depth of the algorithm, although significantly longer than a single Trotter step, does not introduce additional numerical errors to the already noisy simulation results and provides access to simulations over much longer time scales than approximations with error scaling in time. Thus, for calculations which depend on oscillation frequencies, such as the DMFT and other embedding problems, this and other fast-forwarding algorithms may prove valuable in the near term, especially when tailored for hardware connectivity.

ACKNOWLEDGMENTS

T.S. was supported in part by the U.S. Department of Energy, Office of Science, Office of Workforce Development for Teachers and Scientists (WDTS) under the Science Undergraduate Laboratory Internship program. T. K. is supported by the U. S. Department of Energy, Office of Science, Office of Workforce Development for Teachers and Scientists, Office of Science Graduate Student Research (SCGSR) program. The SCGSR program is administered by the Oak Ridge Institute for Science and Education (ORISE) for the DOE. ORISE is managed by ORAU under contract number DE-SC0014664. A.F.K. was supported by the Department of Energy, Office of Basic Energy Sciences, Division of Materials Sciences and Engineering under Grant No. DE-SC0019469. E.F.D. acknowledges DOE ASCR funding under the Quantum Computing Application Teams program, FWP number ERKJ347. Y.W. acknowledges DOE ASCR funding under the Quantum Application Teams program, FWP number ERKJ335. This research used resources of the Oak Ridge Leadership Computing Facility. Access to the IBM Q Network was obtained through the IBM Q Hub at NC State.

DATA AVAILABILITY

Supporting code and data will be made available upon request.

Appendix A: Spin-Fermion Transformation

For digital simulation, we generally employ a mappings from the fermionic operator algebra to the qubit operator algebra composed of Pauli strings: permutations of the Pauli matrices at each qubit site combined via the Kronecker tensor product. The Jordan-Wigner transformation [41] used in this work is one such method. We denote Pauli matrices as $X = \begin{pmatrix} 0 & 1 \\ 1 & 0 \end{pmatrix}$, $Y = \begin{pmatrix} 0 & -i \\ i & 0 \end{pmatrix}$, and $Z = \begin{pmatrix} 1 & 0 \\ 0 & -1 \end{pmatrix}$ and the identity matrix $I = \begin{pmatrix} 1 & 0 \\ 0 & 1 \end{pmatrix}$. The Pauli strings for N -qubit systems are the Kronecker tensor products of N Pauli or identity matrices. We define $Z_i = I^{\otimes(i-1)} \otimes Z \otimes I^{\otimes(N-i)}$ for the type of Pauli strings acting on only a single qubit. The standard procedure follows an algorithm to map the fermionic basis states to the computational basis spanned by a sequence of qubits and the fermionic operators to the sum of Pauli string operators on these qubits. This is given as follows.

1. Map fermionic states to qubit states. We employ a mapping where the spin-orbitals $|i\sigma\rangle$ for the same spin but different sites are grouped together $|0\uparrow, 1\uparrow, \dots, 0\downarrow, 1\downarrow, \dots\rangle$. Occupied states are $|1\rangle$ in the computational basis, and unoccupied states are $|0\rangle$.
2. Apply $\hat{c} \rightarrow \hat{\sigma}_+ = \frac{1}{2}(X + iY)$ and $\hat{c}^\dagger \rightarrow \hat{\sigma}_- = \frac{1}{2}(X - iY)$. From these two identities, we also get $\hat{n} \rightarrow \frac{1}{2}(I - Z)$ and $\hat{h} \rightarrow \frac{1}{2}(I + Z)$.
3. To maintain canonical anticommutation relations for fermion operators $\{\hat{c}_{j\sigma}, \hat{c}_{j'\sigma'}^\dagger\} = \delta_{jj'}\delta_{\sigma\sigma'}$ and $\{\hat{c}_{j\sigma}, \hat{c}_{j'\sigma'}\} = \{\hat{c}_{j\sigma}^\dagger, \hat{c}_{j'\sigma'}^\dagger\} = 0$, map the indexed fermionic operators (site index $0 \leq j \leq N_b$) to the corresponding qubit operators as follows.

$$\begin{aligned}\hat{c}_{j\uparrow} &= \frac{1}{2}Z_1 \cdots Z_{j-1}(X_j + iY_j), & \hat{c}_{j\uparrow}^\dagger &= \frac{1}{2}Z_1 \cdots Z_{j-1}(X_j - iY_j), \\ \hat{c}_{j\downarrow} &= \frac{1}{2}Z_1 \cdots Z_{N_b+j}(X_{N_b+1+j} + iY_{N_b+1+j}), & \hat{c}_{j\downarrow}^\dagger &= \frac{1}{2}Z_1 \cdots Z_{N_b+j}(X_{N_b+1+j} - iY_{N_b+1+j}), \\ \hat{n}_{0\uparrow} &= \frac{1}{2}(I_0 - Z_0), & \hat{n}_{0\downarrow} &= \frac{1}{2}(I_{N_b+1} - Z_{N_b+1}).\end{aligned}$$

In the above, $Z_j \cdots Z_{j'} = \prod_{k=j}^{j'} Z_k$ for $j' \geq j$ and $Z_j \cdots Z_{j'} = 1$ for $j' < j$.

Applying the above steps to the AIM Hamiltonian yields

$$\begin{aligned}\hat{H}_{\text{AIM}} &= \sum_{i=1}^{N_b} \frac{V_i}{2} (X_0 Z_1 \cdots Z_{i-1} X_i + Y_0 Z_1 \cdots Z_{i-1} Y_i \\ &\quad + X_{N_b+1} Z_{N_b+2} \cdots Z_{N_b+i} X_{N_b+1+i} + Y_{N_b+1} Z_{N_b+2} \cdots Z_{N_b+i} Y_{N_b+1+i}) \\ &\quad + \frac{U}{4} (Z_0 Z_{N_b+1} - Z_0 - Z_{N_b+1}) + \sum_{i=0}^{N_b} \frac{\epsilon_i - \mu}{2} (Z_i + Z_{N_b+1+i}).\end{aligned}\tag{A1}$$

We have dropped a constant term $\frac{U}{4} I_0 I_{N_b+1} = \frac{U}{4}$ from the above Hamiltonian since a constant energy shift does not affect the dynamics of a system.

The Hamiltonian simplifies in the two-site case (one impurity site and $N_b = 1$ bath site). Further, due to particle-hole symmetry of a half-filling (total two particles) ground state we will consider, additional constraints on ϵ_0 and ϵ_1 are as follows: the impurity on-site energy $\epsilon_0 = 0$, so $\epsilon_0 - \mu = -\mu = -\frac{U}{2}$; ϵ_1 must satisfy a self-consistency condition in which the occupation of the impurity site is defined by to the occupation of the Hubbard lattice, which results in $\epsilon_1 - \mu = 0$ [32, 33]. Therefore, the simplified two-site \hat{H}_{AIM} with a half-filling ground state is given by

$$\hat{H}_{\text{AIM}} = \frac{V}{2} (X_0 X_1 + Y_0 Y_1 + X_2 X_3 + Y_2 Y_3) + \frac{U}{4} Z_0 Z_2.\tag{A2}$$

Appendix B: Green's function evaluation

The retarded Green's function is given by

$$G_{\text{imp}}^{\text{R}}(t) = \theta(t)[G^>(t) - G^<(t)],$$

where the lesser $G^<(t)$ and greater $G^>(t)$ Green's functions are

$$G^<(t) = i \left\langle \psi_0 \left| \hat{c}_0^\dagger \hat{c}_0(t) \right| \psi_0 \right\rangle,$$

$$G^>(t) = -i \left\langle \psi_0 \left| \hat{c}_0(t) \hat{c}_0^\dagger \right| \psi_0 \right\rangle.$$

Here, $\hat{c}_0(t) = e^{i\hat{H}t} \hat{c}_0 e^{-i\hat{H}t}$ and $\hat{c}_0^\dagger(t) = e^{i\hat{H}t} \hat{c}_0^\dagger e^{-i\hat{H}t}$.

Denote $U(t) = e^{-i\hat{H}t}$ and apply the Jordan-Wigner transform to these terms, we have

$$G^<(t) = i \left\langle \psi_0 \left| \frac{1}{2}(X_0 - iY_0)U^\dagger(t) \frac{1}{2}(X_0 + iY_0)U(t) \right| \psi_0 \right\rangle$$

$$= \frac{i}{4} [\langle X_0 U^\dagger(t) X_0 U(t) \rangle + i \langle X_0 U^\dagger(t) Y_0 U(t) \rangle - i \langle Y_0 U^\dagger(t) X_0 U(t) \rangle + \langle Y_0 U^\dagger(t) Y_0 U(t) \rangle]$$

$$G^>(t) = -i \left\langle \psi_0 \left| U^\dagger(t) \frac{1}{2}(X_0 + iY_0)U(t) \frac{1}{2}(X_0 - iY_0) \right| \psi_0 \right\rangle$$

$$= \frac{-i}{4} [\langle U^\dagger(t) X_0 U(t) X_0 \rangle + i \langle U^\dagger(t) Y_0 U(t) X_0 \rangle - i \langle U^\dagger(t) X_0 U(t) Y_0 \rangle + \langle U^\dagger(t) Y_0 U(t) Y_0 \rangle].$$

Measuring the 8 terms in function $4iG_{\text{imp}}^R(t > 0) = 4i[G^>(t) - G^<(t)] = \langle X_0(t)X_0 \rangle + i \langle Y_0(t)X_0 \rangle - i \langle X_0(t)Y_0 \rangle + \langle Y_0(t)Y_0 \rangle + \langle X_0X_0(t) \rangle + i \langle X_0Y_0(t) \rangle - i \langle Y_0X_0(t) \rangle + \langle Y_0Y_0(t) \rangle$ would require 16 total circuits: two circuits per term for the real and imaginary components, respectively. We reduce the evaluation to only two measurement circuits for real component of the two terms $\langle X_0(t)X_0 \rangle$ and $\langle Y_0(t)Y_0 \rangle$. The simplification follows

$$4iG_{\text{imp}}^R(t > 0)$$

$$= 4i[G^>(t) - G^<(t)]$$

$$= [\langle X_0(t)X_0 \rangle + \langle X_0X_0(t) \rangle] + i[\langle Y_0(t)X_0 \rangle + \langle X_0Y_0(t) \rangle] - i[\langle X_0(t)Y_0 \rangle + \langle Y_0X_0(t) \rangle] + [\langle Y_0(t)Y_0 \rangle + \langle Y_0Y_0(t) \rangle]$$

$$= [\langle X_0(t)X_0 \rangle + \langle X_0(t)X_0 \rangle^*] + i[\langle Y_0(t)X_0 \rangle + \langle Y_0(t)X_0 \rangle^*] - i[\langle X_0(t)Y_0 \rangle + \langle X_0(t)Y_0 \rangle^*] + [\langle Y_0(t)Y_0 \rangle + \langle Y_0(t)Y_0 \rangle^*]$$

$$= 2 \text{Re} \langle X_0(t)X_0 \rangle + 2i \text{Re} \langle Y_0(t)X_0 \rangle - 2i \text{Re} \langle X_0(t)Y_0 \rangle + 2 \text{Re} \langle Y_0(t)Y_0 \rangle.$$

Since at half-filling, due to particle-hole symmetry, the imaginary component of $iG_{\text{imp}}^R(t)$ is zero, we only need to measure the first and last term in the above: the real components $\text{Re} \langle X_0(t)X_0 \rangle$ and $\text{Re} \langle Y_0(t)Y_0 \rangle$.

Appendix C: Singular behavior of self-energy and its derivative at zero frequency

We will drop the impurity “imp” subscript for simplicity below. To extract the poles $\omega = \omega_{1,2}$ and pole strength $\alpha_{1,2}$ of the retarded interacting impurity Green's function

$$G(\omega) = \frac{\alpha_1}{\omega - \omega_1 + i0^+} + \frac{\alpha_1}{\omega + \omega_1 + i0^+} + \frac{\alpha_2}{\omega - \omega_2 + i0^+} + \frac{\alpha_2}{\omega + \omega_2 + i0^+} \quad (\text{C1})$$

the following function form is used to fit $G(t)$ simulated and measured on quantum computer:

$$iG(t > 0) = \alpha_1 e^{i\omega_1 t} + \alpha_1 e^{-i\omega_1 t} + \alpha_2 e^{i\omega_2 t} + \alpha_2 e^{-i\omega_2 t} = 2\alpha_1 \cos(\omega_1 t) + 2\alpha_2 \cos(\omega_2 t). \quad (\text{C2})$$

$$\Sigma(\omega) = \frac{1}{G^{(0)}(\omega)} - \frac{1}{G(\omega)}, \quad (\text{C3})$$

$$\frac{d\Sigma(\omega)}{d\omega} = -\frac{dG^{(0)}(\omega)/d\omega}{[G^{(0)}(\omega)]^2} + \frac{dG(\omega)/d\omega}{[G(\omega)]^2}. \quad (\text{C4})$$

$$G^{(0)}(\omega) = \frac{1/2}{\omega - V} + \frac{1/2}{\omega + V}, \quad (\text{C5})$$

$$G(\omega) = \frac{\alpha_1}{\omega - \omega_1} + \frac{\alpha_1}{\omega + \omega_1} + \frac{\alpha_2}{\omega - \omega_2} + \frac{\alpha_2}{\omega + \omega_2}. \quad (\text{C6})$$

$$G^{(0)}(\omega)\Big|_{\omega=0} = 1/(-2V) + 1/(2V) = 0.$$

$$\frac{dG^{(0)}(\omega)}{d\omega} = -\frac{1}{2(\omega - V)^2} - \frac{1}{2(\omega + V)^2}, \quad (\text{C7})$$

$$\frac{dG(\omega)}{d\omega} = -\frac{\alpha_1}{(\omega - \omega_1)^2} - \frac{\alpha_1}{(\omega + \omega_1)^2} - \frac{\alpha_2}{(\omega - \omega_2)^2} - \frac{\alpha_2}{(\omega + \omega_2)^2}, \quad (\text{C8})$$

$$\begin{aligned} \frac{d\Sigma(\omega)}{d\omega} &= -\frac{dG^{(0)}(\omega)/d\omega}{G_0^2(\omega)} + \frac{dG(\omega)/d\omega}{G^2(\omega)} \\ &= \frac{\frac{1/2}{(\omega - V)^2} + \frac{1/2}{(\omega + V)^2}}{\left(\frac{1/2}{\omega - V} + \frac{1/2}{\omega + V}\right)^2} - \frac{\frac{\alpha_1}{(\omega - \omega_1)^2} + \frac{\alpha_1}{(\omega + \omega_1)^2} + \frac{\alpha_2}{(\omega - \omega_2)^2} + \frac{\alpha_2}{(\omega + \omega_2)^2}}{\left(\frac{\alpha_1}{\omega - \omega_1} + \frac{\alpha_1}{\omega + \omega_1} + \frac{\alpha_2}{\omega - \omega_2} + \frac{\alpha_2}{\omega + \omega_2}\right)^2} \\ &= \frac{\omega^2 + V^2}{\omega^2} - \frac{\alpha_1(\omega^2 - \omega_2^2)^2(\omega^2 + \omega_1^2) + \alpha_2(\omega^2 - \omega_1^2)^2(\omega^2 + \omega_2^2)}{2\omega^2[\alpha_1(\omega^2 - \omega_2^2) + \alpha_2(\omega^2 - \omega_1^2)]^2} \\ &= 1 + \frac{V^2}{\omega^2} - \frac{\alpha_1(\omega^2 - \omega_2^2)^2 + \alpha_2(\omega^2 - \omega_1^2)^2}{2[\alpha_1(\omega^2 - \omega_2^2) + \alpha_2(\omega^2 - \omega_1^2)]^2} - \frac{\alpha_1(\omega^2 - \omega_2^2)^2\omega_1^2 + \alpha_2(\omega^2 - \omega_1^2)^2\omega_2^2}{2\omega^2[\alpha_1(\omega^2 - \omega_2^2) + \alpha_2(\omega^2 - \omega_1^2)]^2}. \end{aligned} \quad (\text{C9})$$

$$\Sigma'(\omega) = -\frac{1}{\omega^2} \left\{ \frac{\alpha_1(\omega^2 - \omega_2^2)^2\omega_1^2 + \alpha_2(\omega^2 - \omega_1^2)^2\omega_2^2}{2[\alpha_1(\omega^2 - \omega_2^2) + \alpha_2(\omega^2 - \omega_1^2)]^2} - V^2 \right\} + 1 - \frac{\alpha_1(\omega^2 - \omega_2^2)^2 + \alpha_2(\omega^2 - \omega_1^2)^2}{2[\alpha_1(\omega^2 - \omega_2^2) + \alpha_2(\omega^2 - \omega_1^2)]^2} \quad (\text{C10})$$

$$\equiv -\frac{1}{x} \left[\frac{f(x)}{g(x)} - V^2 \right] + h(x). \quad (\text{C11})$$

In the last step, we have defined functions $f(x) = \alpha_1(x - x_2)^2x_1 + \alpha_2(x - x_1)^2x_2$, $g(x) = 2[\alpha_1(x - x_2) + \alpha_2(x - x_1)]^2$, and $h(x) = 1 - [\alpha_1(x - x_2)^2 + \alpha_2(x - x_1)^2]/g(x)$, where $x = \omega^2$, $x_1 = \omega_1^2$, and $x_2 = \omega_2^2$, for the discussion below. Before making any further simplification, we check the consistency of Eq. (C10).

- First check, for $U = 0$, $\alpha_1 = 1/2$, $\alpha_2 = 0$, $\omega_1 = V$. From Eqs. (C3) and Eq. (C6), we find $\Sigma(\omega) = 0$ and $\Sigma'(\omega) = \frac{d\Sigma(\omega)}{d\omega} = 0$. Plugging $\alpha_1 = 1/2$, $\alpha_2 = 0$, $\omega_1 = V$ into Eq. (C10), we also find $\Sigma'(\omega) = 0$.
- Second check, for $V = 0$ (this is the so-called atomic limit — the “atom” is the single impurity site), $\alpha_1 = 0$, $\alpha_2 = 1/2$, $\omega_1 = 0$ and $\omega_2 = U/2$. From Eqs. (C3) and Eq. (C6), we find $\Sigma(\omega) = (\frac{1}{\omega})^{-1} - (\frac{1}{2\omega - U} + \frac{1}{2\omega + U})^{-1} = \omega - \frac{4\omega^2 - U^2}{4\omega} = \frac{U^2}{4\omega}$ and $\Sigma'(\omega) = \frac{d\Sigma(\omega)}{d\omega} = -\frac{U^2}{4\omega^2}$. Plugging $\alpha_1 = 0$, $\alpha_2 = 1/2$, $\omega_2 = U/2$ into Eq. (C10), we also find $\Sigma'(\omega) = -\frac{\omega_2^2}{\omega^2} = -\frac{U^2}{4\omega^2}$.

Now we derive a more stable formula to calculate $\lim_{\omega \rightarrow 0} \frac{d\Sigma(\omega)}{d\omega} \equiv \Sigma'(0)$. First, $h(x)|_{x=\omega^2=0}$ is finite because if the denominator of the second term in $h(x)$ is zero at $x = \omega^2 = 0$, this implies that $\alpha_1\omega_2^2 + \alpha_2\omega_1^2 = 0$, which is impossible since $\alpha_1, \alpha_2, \omega_1, \omega_2 \geq 0$, $\alpha_1 + \alpha_2 > 0$, and $\omega_1 + \omega_2 > 0$. Therefore, the first term of $\Sigma'(\omega)$, $-\frac{1}{x} \left[\frac{f(x)}{g(x)} - V^2 \right]$, must also be finite as $x = \omega^2 \rightarrow 0$. This is only possible if $\frac{f(x)}{g(x)} - V^2 \Big|_{x=0} = 0$, which gives

$$\frac{f(x)}{g(x)} \Big|_{x=0} = \frac{f(0)}{g(0)} = \frac{\alpha_1x_2^2x_1 + \alpha_2x_1^2x_2}{2(\alpha_1x_2 + \alpha_2x_1)^2} = \frac{x_1x_2(\alpha_1x_2 + \alpha_2x_1)}{2(\alpha_1x_2 + \alpha_2x_1)^2} = \frac{x_1x_2}{2(\alpha_1x_2 + \alpha_2x_1)} = V^2. \quad (\text{C12})$$

Therefore, we can evaluate the $x \rightarrow 0$ limit of the first term $-\frac{1}{x} \left[\frac{f(x)}{g(x)} - V^2 \right]$ with L'Hôpital's rule as follows.

$$\begin{aligned} \lim_{x \rightarrow 0} -\frac{1}{x} \left[\frac{f(x)}{g(x)} - V^2 \right] &= \lim_{x \rightarrow 0} \frac{g(x)V^2 - f(x)}{xg(x)} = \lim_{x \rightarrow 0} \frac{d[g(x)V^2 - f(x)]/dx}{d[xg(x)]/dx} \\ &= \lim_{x \rightarrow 0} \frac{g'(x)V^2 - f'(x)}{g(x) + xg'(x)} = \frac{g'(0)V^2 - f'(0)}{g(0)}. \end{aligned} \quad (\text{C13})$$

$$f(x) = \alpha_1(x - x_2)^2x_1 + \alpha_2(x - x_1)^2x_2,$$

$$f'(x) = 2\alpha_1(x - x_2)x_1 + 2\alpha_2(x - x_1)x_2,$$

$$f'(0) = -2x_1x_2(\alpha_1 + \alpha_2) = -4V^2(\alpha_1x_2 + \alpha_2x_1)(\alpha_1 + \alpha_2). \quad [\text{see Eq. (C12)}]$$

$$\begin{aligned}
g(x) &= 2[\alpha_1(x - x_2) + \alpha_2(x - x_1)]^2, \\
g'(x) &= 4[\alpha_1(x - x_2) + \alpha_2(x - x_1)](\alpha_1 + \alpha_2), \\
g'(0) &= -4(\alpha_1 x_2 + \alpha_2 x_1)(\alpha_1 + \alpha_2). \\
\therefore \lim_{x \rightarrow 0} -\frac{1}{x} \left[\frac{f(x)}{g(x)} - V^2 \right] &= \frac{g'(0)V^2 - f'(0)}{g(0)} \\
&= \frac{-4V^2(\alpha_1 x_2 + \alpha_2 x_1)(\alpha_1 + \alpha_2) + 4V^2(\alpha_1 x_2 + \alpha_2 x_1)(\alpha_1 + \alpha_2)}{g(0)} = 0.
\end{aligned} \tag{C14}$$

Since the first term of $\Sigma'(\omega)$, Eq. (C14), is zero, we find

$$\left. \frac{d\Sigma(\omega)}{d\omega} \right|_{\omega=0} = h(0) = 1 - \frac{\alpha_1 x_2^2 + \alpha_2 x_1^2}{2(\alpha_1 x_2 + \alpha_2 x_1)^2}, \tag{C15}$$

$$\begin{aligned}
\mathcal{Z} &= 1 \left/ \left[1 - \frac{d\text{Re}\Sigma(\omega)}{d\omega} \right] \right|_{\omega=0} = \frac{2(\alpha_1 x_2 + \alpha_2 x_1)^2}{\alpha_1 x_2^2 + \alpha_2 x_1^2}, \\
x_1 &= \omega_1^2, \quad x_2 = \omega_2^2.
\end{aligned} \tag{C16}$$

Eqs. (C15) and (C16) are more stable and robust against numerical or (quantum) simulation error comparing to the analytical formula Eq. (C10) for the derivative $\frac{d\Sigma(\omega)}{d\omega}$ or a numerical implementation:

$$\frac{d\Sigma(\omega)}{d\omega} \approx \frac{[1/G^{(0)}(\Delta\omega) - 1/G(\Delta\omega)] - [1/G^{(0)}(-\Delta\omega) - 1/G(-\Delta\omega)]}{2\Delta\omega}.$$

The stability comes from the removal of the first term in Eq. (C10) which is mathematically singular if the condition Eq. (C12) is not satisfied exactly. Numerically, adding a small imaginary part to the frequency $\omega \rightarrow \omega + i\delta$ or using a finite step size $\Delta\omega$ in the derivative calculation might reduce the divergence but this is less stable than using Eqs. (C15) and (C16).

Last, we can strictly enforce the two conditions $\alpha_1 + \alpha_2 = \frac{1}{2}$ and Eq. (C12) $\frac{\alpha_1}{x_1} + \frac{\alpha_2}{x_2} = \frac{1}{2V^2}$ in Eqs. (C15) and (C16) to further improve accuracy. The two conditions can be enforced during the parameter fitting step, but this is not required since in the following equations, we use $\alpha_1 + \alpha_2 = \frac{1}{2}$ and $\frac{\alpha_1}{x_1} + \frac{\alpha_2}{x_2} = \frac{1}{2V^2}$ to eliminate the less accurate fitting parameters ω_1 and α_1 when V is small or $V \rightarrow 0$ in the DMFT self-consistent loop calculation for insulating phase. In this case, $\alpha_1 \rightarrow 0$, $\alpha_2 \rightarrow \frac{1}{2}$, $\omega_2 \rightarrow \frac{U}{2}$, $x_2 \rightarrow \omega_2^2 \rightarrow \frac{U^2}{4}$, so $\frac{\alpha_2}{x_2} \rightarrow \frac{2}{U^2}$ and $\frac{\alpha_1}{x_1} \rightarrow \frac{1}{2V^2} - \frac{2}{U^2}$.

$$\begin{aligned}
\mathcal{Z} &= \frac{2(\alpha_1 x_2 + \alpha_2 x_1)^2}{\alpha_1 x_2^2 + \alpha_2 x_1^2} = \frac{2\left(\frac{\alpha_1}{x_1} + \frac{\alpha_2}{x_2}\right)^2}{\frac{\alpha_1^2}{x_1^2} + \frac{\alpha_2^2}{x_2^2}} \\
&= \frac{\frac{1}{2V^4}}{\frac{\alpha_1^2}{x_1^2} \frac{1}{\alpha_1} + \frac{\alpha_2^2}{x_2^2}} \xrightarrow{V \rightarrow 0} \frac{2\alpha_1}{4V^4 \left(\frac{1}{2V^2} - \frac{2}{U^2} + o(1)\right)^2 + 4V^4 \alpha_1 \frac{\alpha_2}{x_2^2}} \\
&\xrightarrow{V \rightarrow 0} \frac{2\alpha_1}{4V^4 \left(\frac{1}{4V^4} - \frac{2}{V^2 U^2} + O(1)\right) + O(V^4)} \\
&= 2\alpha_1 \left(1 + \frac{8V^2}{U^2} + O(V^4)\right) = (1 - 2\alpha_2) \left(1 + \frac{8V^2}{U^2} + O(V^4)\right).
\end{aligned} \tag{C17}$$

The final Eq. (C17) is equivalent to the \mathcal{Z} obtained from integrating the spectral function $\int_{-\omega_1^+}^{\omega_1^+} d\omega A(\omega) = \int_{-\omega_1^+}^{\omega_1^+} d\omega [\alpha_1 \delta(\omega - \omega_1) + \alpha_1 \delta(\omega + \omega_1)] = 2\alpha_1$.

Alternatively, we can use the two conditions

$$\alpha_1 + \alpha_2 = \frac{1}{2} \tag{C18a}$$

$$x_2 \alpha_1 + x_1 \alpha_2 = \frac{x_1 x_2}{2V^2} \tag{C18b}$$

to solve for α_1 and α_2 in terms of x_1 , x_2 , and V , and then eliminate them from the Eq. (C16). The final result is

$$\mathcal{Z} = \frac{x_1 x_2}{V^2(x_1 + x_2 - V^2)} = \frac{\omega_1^2 \omega_2^2}{V^2(\omega_1^2 + \omega_2^2 - V^2)}. \quad (\text{C19})$$

In practice, for $U \lesssim U_c$, the following formula using only the parameters $(\alpha_1/\alpha_2, \omega_2, V)$ might be more suitable to calculate \mathcal{Z} from self-energy derivative:

$$\mathcal{Z} = \frac{\alpha_1/\alpha_2}{(\alpha_1/\alpha_2) + (1 - V^2/\omega_2^2)^2}. \quad (\text{C20})$$

Appendix D: Quantum Hardware:

The quantum hardware used in this work was `ibmq_manila`, a 5 qubit superconducting device which is publicly available through the IBM Quantum Experience. The experiment parameters are designed around the open access quantum job submission limits of 5 sets of 75 circuit evaluations of 8,192 shots each. Thus, we used two iterations of the Cartan parameters which combine to a total shot count of 16,000 at each of 150 time step evaluations. The first set was reserved for just in time measurement error mitigation circuits, of which there are 32 circuits preparing each of the 2^5 computational basis states. Assuming a correct evaluation, each DMFT Loop requires approximately 36 minutes to execute on the IBM backend, including the Measurement Error Mitigation circuits. In practice, the update failure condition results in repeated calculations and subsequently increased run-times for each V update. Tables I and II show the qubit coherence times and the entangling gate properties, respectively. The ancilla qubit was placed at index 0. Calibration data pulled from the Qiskit API, and averaged by taking the calibration data at 4 points each day between October 10th 2021 and November 10th 2021 [36].

Qubit Number	T1 (μs)	T2 (μs)
0 (Ancilla)	146.18 \pm 29.78	94.38 \pm 18.50
1	204.64 \pm 47.57	83.02 \pm 15.18
2	148.79 \pm 26.79	24.30 \pm 2.55
3	157.19 \pm 36.33	63.64 \pm 7.83
4	128.96 \pm 24.11	42.78 \pm 2.57

TABLE I: Average T1 and T2 coherence times for `ibmq_manila`, averaged over the period of time in which runs were executed.

Connection	CNOT Fidelity	Gate Timing (ns)
0-1	0.0070 \pm 0.0012	295.11 \pm 17.78
1-2	0.0099 \pm 0.0017	487.11 \pm 17.78
2-3	0.0071 \pm 0.00080	373.33 \pm 17.78
3-4	0.0076 \pm 0.0016	316.44 \pm 17.78

TABLE II: Average CNOT fidelity and gate timings on `imbq_manila`.

-
- [1] P. W. Shor, Polynomial-time algorithms for prime factorization and discrete logarithms on a quantum computer, *SIAM Journal on Computing* **26**, 1484–1509 (1997).
 - [2] B. Bauer, D. Wecker, A. J. Millis, M. B. Hastings, and M. Troyer, Hybrid quantum-classical approach to correlated materials, *Physical Review X* **6**, 1 (2016).
 - [3] I. D. Kivlichan, J. McClean, N. Wiebe, C. Gidney, A. Aspuru-Guzik, G. K. L. Chan, and R. Babbush, Quantum Simulation of Electronic Structure with Linear Depth and Connectivity, *Physical Review Letters* **120**, 110501 (2018).
 - [4] Z. Jiang, K. J. Sung, K. Kechedzhi, V. N. Smelyanskiy, and S. Boixo, Quantum Algorithms to Simulate Many-Body Physics of Correlated Fermions, *Physical Review Applied* **9**, 44036 (2018).

- [5] D. Wecker, M. B. Hastings, N. Wiebe, B. K. Clark, C. Nayak, and M. Troyer, Solving strongly correlated electron models on a quantum computer, *Physical Review A - Atomic, Molecular, and Optical Physics* **92**, 1 (2015).
- [6] N. M. Linke, S. Johri, C. Figgatt, K. A. Landsman, A. Y. Matsuura, and C. Monroe, Measuring the Rényi entropy of a two-site Fermi-Hubbard model on a trapped ion quantum computer, *Physical Review A* **98**, 10.1103/PhysRevA.98.052334 (2018).
- [7] I. Rungger, N. Fitzpatrick, H. Chen, C. H. Alderete, H. Apel, A. Cowtan, A. Patterson, D. M. Ramo, Y. Zhu, N. H. Nguyen, E. Grant, S. Chretien, L. Wossnig, N. M. Linke, and R. Duncan, Dynamical mean field theory algorithm and experiment on quantum computers (2019), [arXiv:arXiv:1910.04735](https://arxiv.org/abs/1910.04735).
- [8] T. Keen, T. Maier, S. Johnston, and P. Lougovski, Quantum-classical simulation of two-site dynamical mean-field theory on noisy quantum hardware, *Quantum Science and Technology* **5**, 035001 (2020).
- [9] B. Jaderberg, A. Agarwal, K. Leonhardt, M. Kiffner, and D. Jaksch, Minimum hardware requirements for hybrid quantum-classical dmft, *Quantum Science and Technology* **5**, 034015 (2020).
- [10] E. Kökcü, T. Steckmann, J. K. Freericks, E. F. Dumitrescu, and A. F. Kemper, Fixed depth Hamiltonian simulation via Cartan decomposition, [arXiv:2104.00728](https://arxiv.org/abs/2104.00728) [cond-mat, physics:quant-ph] (2021).
- [11] N. F. MOTT, Metal-insulator transition, *Rev. Mod. Phys.* **40**, 677 (1968).
- [12] M. Imada, A. Fujimori, and Y. Tokura, Metal-insulator transitions, *Rev. Mod. Phys.* **70**, 1039 (1998).
- [13] A. Georges and G. Kotliar, Hubbard model in infinite dimensions, *Phys. Rev. B* **45**, 6479 (1992).
- [14] S. R. White, D. J. Scalapino, R. L. Sugar, E. Y. Loh, J. E. Gubernatis, and R. T. Scalettar, Numerical study of the two-dimensional hubbard model, *Phys. Rev. B* **40**, 506 (1989).
- [15] B.-X. Zheng, C.-M. Chung, P. Corboz, G. Ehlers, M.-P. Qin, R. M. Noack, H. Shi, S. R. White, S. Zhang, and G. K.-L. Chan, Stripe order in the underdoped region of the two-dimensional hubbard model, *Science* **358**, 1155 (2017).
- [16] E. W. Huang, C. B. Mendl, H.-C. Jiang, B. Moritz, and T. P. Devereaux, Stripe order from the perspective of the hubbard model, *npj Quantum Materials* **3**, 22 (2018).
- [17] E. W. Huang, R. Sheppard, B. Moritz, and T. P. Devereaux, Strange metallicity in the doped hubbard model, *Science* **366**, 987 (2019).
- [18] E. Gull, O. Parcollet, and A. J. Millis, Superconductivity and the pseudogap in the two-dimensional hubbard model, *Phys. Rev. Lett.* **110**, 216405 (2013).
- [19] X. Chen, J. P. F. LeBlanc, and E. Gull, Superconducting fluctuations in the normal state of the two-dimensional hubbard model, *Phys. Rev. Lett.* **115**, 116402 (2015).
- [20] T. A. Maier, M. Jarrell, T. C. Schulthess, P. R. C. Kent, and J. B. White, Systematic study of d -wave superconductivity in the 2d repulsive hubbard model, *Phys. Rev. Lett.* **95**, 237001 (2005).
- [21] J. Hubbard, Electron correlations in narrow energy bands, *Proceedings of the Royal Society of London. Series A. Mathematical and Physical Sciences* **276**, 238 (1963).
- [22] D. Wecker, M. B. Hastings, and M. Troyer, Progress towards practical quantum variational algorithms, *Physical Review A - Atomic, Molecular, and Optical Physics* **92**, 1 (2015).
- [23] J.-M. Reiner, F. Wilhelm-Mauch, G. Schön, and M. Marthaler, Finding the ground state of the Hubbard model by variational methods on a quantum computer with gate errors, *Quantum Science and Technology* **4**, 035005 (2019).
- [24] I. D. Kivlichan, C. Gidney, D. W. Berry, N. Wiebe, J. McClean, W. Sun, Z. Jiang, N. Rubin, A. Fowler, A. Aspuru-Guzik, H. Neven, and R. Babbush, Improved Fault-Tolerant Quantum Simulation of Condensed-Phase Correlated Electrons via Trotterization, *Quantum* **4**, 296 (2020).
- [25] D. Wecker, M. B. Hastings, N. Wiebe, B. K. Clark, C. Nayak, and M. Troyer, Solving strongly correlated electron models on a quantum computer, *Physical Review A - Atomic, Molecular, and Optical Physics* **92**, 1 (2015).
- [26] P. Lunts, A. Georges, E. M. Stoudenmire, and M. Fishman, The hubbard model on the bethe lattice via variational uniform tree states: metal-insulator transition and a fermi liquid, *Physical Review Research* **3**, 023054 (2021), [arXiv: 2010.06543](https://arxiv.org/abs/2010.06543).
- [27] G. Kotliar and D. Vollhardt, Strongly correlated materials: Insights from dynamical mean-field theory, *Physics Today* **57**, 53 (2004).
- [28] A. Liebsch and H. Ishida, Temperature and bath size in exact diagonalization dynamical mean field theory, *Journal of Physics Condensed Matter* **24**, 10.1088/0953-8984/24/5/053201 (2012).
- [29] E. Gull, A. J. Millis, A. I. Lichtenstein, A. N. Rubtsov, M. Troyer, and P. Werner, Continuous-time monte carlo methods for quantum impurity models, *Rev. Mod. Phys.* **83**, 349 (2011).
- [30] F. A. Wolf, I. P. McCulloch, and U. Schollwöck, Solving nonequilibrium dynamical mean-field theory using matrix product states, *Phys. Rev. B* **90**, 235131 (2014).
- [31] M. Troyer and U.-J. Wiese, Computational complexity and fundamental limitations to fermionic quantum monte carlo simulations, *Physical Review Letters* **94**, 10.1103/physrevlett.94.170201 (2005).
- [32] M. Potthoff, Two-site dynamical mean-field theory, *Physical Review B* **64**, 165114 (2001).
- [33] J. M. Kreula, L. García-Álvarez, L. Lamata, S. R. Clark, E. Solano, and D. Jaksch, Few-qubit quantum-classical simulation of strongly correlated lattice fermions, *EPJ Quantum Technology* **3**, 1 (2016).
- [34] H. N. Sá Earp and J. K. Pachos, A constructive algorithm for the Cartan decomposition of $SU(2^N)$, *Journal of Mathematical Physics* **46**, 082108 (2005).
- [35] T. Steckmann and E. Kökcü, (2021), Cartan Quantum Synthesizer: <https://github.com/kemperlab/cartan-quantum-synthesizer>.
- [36] M. S. ANIS *et al.*, Qiskit: An open-source framework for quantum computing (2021).
- [37] B. Zhang, S. Majumder, P. H. Leung, S. Crain, Y. Wang, C. Fang, D. M. Debroy, J. Kim, and K. R. Brown, Hidden Inverses: Coherent Error Cancellation at the Circuit Level, [arXiv:2104.01119](https://arxiv.org/abs/2104.01119) [quant-ph] (2021), [arXiv: 2104.01119](https://arxiv.org/abs/2104.01119).

- [38] A. Asfaw, A. Corcoles, L. Bello, Y. Ben-Haim, M. Bozzo-Rey, S. Bravyi, N. Bronn, L. Capelluto, A. C. Vazquez, J. Ceroni, R. Chen, A. Frisch, J. Gambetta, S. Garion, L. Gil, S. D. L. P. Gonzalez, F. Harkins, T. Imamichi, H. Kang, A. h. Karamlou, R. Lored, D. McKay, A. Mezzacapo, Z. Mineev, R. Movassagh, G. Nannicini, P. Nation, A. Phan, M. Pistoia, A. Rattew, J. Schaefer, J. Shabani, J. Smolin, J. Stenger, K. Temme, M. Tod, S. Wood, and J. Wootton., [Learn quantum computation using qiskit](#) (2020).
- [39] B. Shaparenko and J. M. Cimbala, A simple equation for predicting aliasing frequency, (in press) *International Journal of Mechanical Engineering Education* (2012).
- [40] E. Lange, Renormalized vs unrenormalized perturbation-theoretical approaches to the mott transition, [Modern Physics Letters B](#) **12**, 915–919 (1998), arXiv: cond-mat/9810208.
- [41] M. A. Nielsen, [The fermionic canonical commutation relations and the Jordan-Wigner transform](#) (2005), unpublished.